Aerodynamic Installation Effects of Lateral Rotors on a Novel Compound Helicopter Configuration

Tom Stokkermans
PhD Candidate
Delft University of Technology
Delft, the Netherlands

Mark Voskuijl
Assistant Professor
Delft University of Technology
Delft, the Netherlands

Leo Veldhuis
Full Professor
Delft University of Technology
Delft, the Netherlands

Bambang Soemarwoto
Senior Scientist
Netherlands Aerospace Centre NLR
Amsterdam, the Netherlands

Raphaël Fukari
Engineer
Airbus Helicopters
Marignane, France

Paul Eglin
Aeromechanics senior expert
Airbus Helicopters
Marignane, France

ABSTRACT

Installation effects of the lateral rotors for a compound helicopter were investigated by means of unsteady CFD simulations. The helicopter featured a box-wing design for additional lift in cruise and wingtip-mounted lateral rotors in pusher configuration for additional thrust in cruise and counter-torque in hover. It was found that propeller performance installation effects for a compound helicopter are highly beneficial in cruise, while some penalties exist in extreme and specific cases in hover and autorotation. In cruise the main interaction was between the wing and lateral rotors, resulting in a propulsive efficiency increase up to 10.6% due to wingtip vortex energy recovery. In hover the main rotor slipstream resulted in a near perpendicular inflow to the lateral rotors, with a disturbance from the wings due to the deflection of the main rotor slipstream. For higher than nominal lateral rotor thrust settings, this resulted in a performance penalty. In autorotation a small power installation penalty was present due to inflow disturbances.

NOTATION

C_D	Drag coefficient
C_L	Lift coefficient
C_P	Power coefficient $C_P = {}^{P}/_{\rho_\infty n^3 D_p^5}$
C_p	Pressure coefficient
C_T	Thrust coefficient $C_T = {}^{T}/_{\rho_\infty n^2 D_p^4}$
c	Chord
D_p	Propeller diameter
E	Richardson extrapolation uncertainty
h_{hover}	Hover altitude
L	CFD domain length
n	Rotational speed
P	Shaft power
q	Dynamic pressure
R	Radius
r	Radial coordinate
T	Thrust
V	Velocity
V_d	Downwash farfield velocity $V_d = \sqrt{{}^{2T_{\text{mr}}}/_{\rho_\infty \pi R_{\text{mr}}^2}}$
y^+	Dimensionless wall distance

Greek

α	Angle of attack
Δp_t	Total pressure difference w.r.t. freestream
δ_f	Flap deflection
η_p	Propulsive efficiency $\eta_p = {}^{TV_\infty}/_{P}$
φ	Blade phase angle

Subscripts

a	Axial
inst	Installed
iso	Isolated
mr	Main rotor
p	Propeller
t	Tangential
∞	Freestream

INTRODUCTION

A compound helicopter is a helicopter where the function of the main rotor of providing lift and thrust is supported by different means. Following Yeo and Johnson (Ref. 1) compounding can be split in lift compounding by the addition of wings to the fuselage and thrust compounding by the addition of propulsive devices. Combined lift and thrust compounding is often called full compounding. The goal is to expand the flight envelope, especially improve the high speed capability of the helicopter while maintaining a helicopters efficient hover advantage over fixed wing aircraft.

As part of the Clean Sky 2 (CS2) research programme, the

Presented at the AHS International 74th Annual Forum & Technology Display, Phoenix, Arizona, USA, May 14–17, 2018.

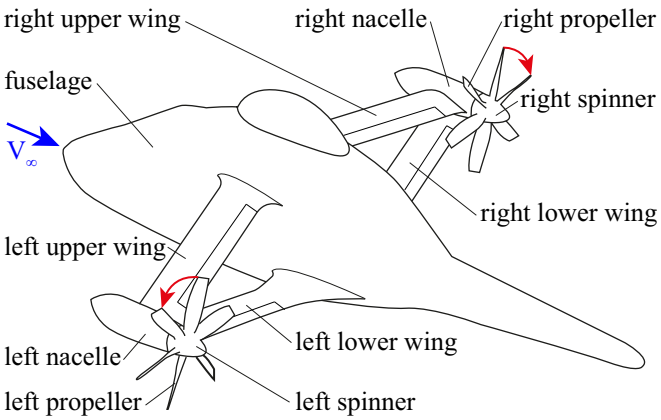

Fig. 1: Sketch of the Airbus RACER without tailplanes.

Airbus RACER (Rapid And Cost-Effective Rotorcraft) is being developed. This full compound helicopter design is optimized for a cruise speed of 220 kts (Ref. 2). Figure 1 shows a sketch of the helicopter with its tailplanes removed. Additional lift in the cruise condition is provided by a box-wing design, while wingtip-mounted lateral rotors in pusher configuration provide additional thrust in the cruise condition and counter-torque in the hover condition. The box-wing design reduces the overall surface affected by the downwash from the main rotor in hover while providing the required lift in cruise. As part of the CS2 PROPTER project (Support to aerodynamic analysis and design of propellers of a compound helicopter), this paper investigates the effects of installation on the lateral rotor performance, focusing on the aerodynamic interaction with the box-wings and main rotor slipstream. For this research an extensive amount of unsteady Reynolds-averaged Navier-Stokes (RANS) CFD simulations have been performed. Comparison with simulation results of the isolated propellers provides the necessary insight into the propeller installation effects. For improved reading of the paper the lateral rotors will be referred to as *propellers*.

In the cruise condition the aerodynamic interaction between the main rotor and propellers is limited since their slipstreams are separated, as sketched in Figure 2 (a). Orchard and Newman (Ref. 3) underline that propellers are particularly advantageous as propulsion device for compound helicopters considering their high efficiency at the moderate cruising speed. An additional efficiency advantage for these propellers can be expected because of the installation on the wingtip in pusher configuration, potentially resulting in wingtip vortex energy recovery by the propellers and wing induced drag reduction (Refs. 4–6). The impact of the novel box-wings on these efficiency benefits is investigated in this paper, including the effect of trailing edge flap deflection on all four wing halves. These flaps allow a change in the ratio of wing lift to main rotor lift in forward flight.

Although propellers may be beneficial in the cruise condition where the main rotor slipstream generally passes over them, the lack of shielding of the propellers may pose a problem at low airspeed and particularly in the hover condition where the main rotor slipstream impinges on the propellers as sketched in Figure 2 (b). Bending moments of the propeller blades due to this skewed inflow may be significant (Ref. 3). Furthermore, a propeller close to the main rotor may affect the rotor flapping amplitude and bending moments due to its pressure field, as is known from the extensive experimental investigation of Bain and Landgrebe (Ref. 7). Not only the propellers but also the wings experience a large variation of angle of attack in the flight envelope as shown by Lynn (Ref. 8). The wings may cause an additional disturbance to the inflow of the propellers. Because of these unknowns, the impact of this complex interactional flow on the propeller performance and unsteady aerodynamic loading is investigated. This will provide the necessary insight for mitigation of possible problems by propeller blade shape optimisation.

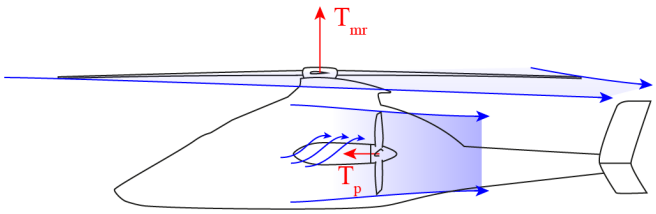

(a) Interaction in the cruise condition.

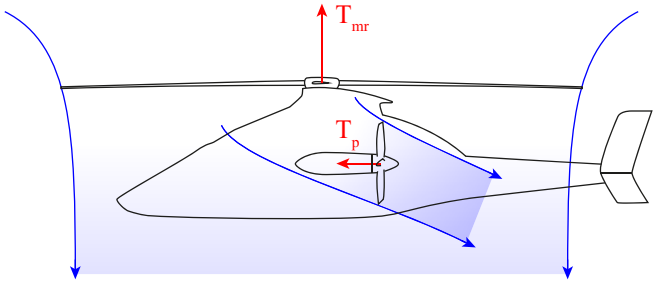

(b) Interaction in the hover condition.

Fig. 2: Main rotor and propeller aerodynamic interaction.

Furthermore, at low speed conditions the right propeller needs to provide reverse thrust for counter-torque. Reverse propeller thrust flow phenomena are not well described in literature, apart from the experimental investigation by Roosenboom and Schröder (Ref. 9). This paper provides some insight in reverse thrust performance effects for compound helicopters.

COMPUTATIONAL SETUP

A perspective view of the simulated body is sketched in Figure 1. The helicopter fuselage with box-wings was simulated with two fully resolved six-bladed tip-mounted propellers turning inboard-up, all represented by no-slip walls. All four wing halves were equipped with plain flaps over the majority of the span. In the remainder of the paper this body without the propeller blades is referred to as the *airframe*. The model was simplified by removal of the tailplanes and the time-averaged effect of the main rotor was introduced by an actuator disk implementation that introduces radially and circumferentially varying momentum and energy jump conditions based on provided blade loading distributions. The domain for the cruise

and autorotation condition and the enlarged domain for the hover condition are sketched in Figure 3. For the cruise and autorotation condition the dimension in the freestream direction L was chosen larger than the other dimensions to diminish the effect of the boundary conditions on the flowfield near the helicopter. Furthermore, on all boundaries, general free stream boundary conditions were prescribed based on Riemann invariants. For the hover condition a larger domain was required to prevent unwanted recirculation and thus unwanted influence of the boundary conditions on the flowfield near the helicopter. The bottom boundary condition was placed at a distance equal to the hover altitude h_{hover} and modelled as a slip wall. A very small freestream velocity was prescribed to further reduce recirculation in the domain.

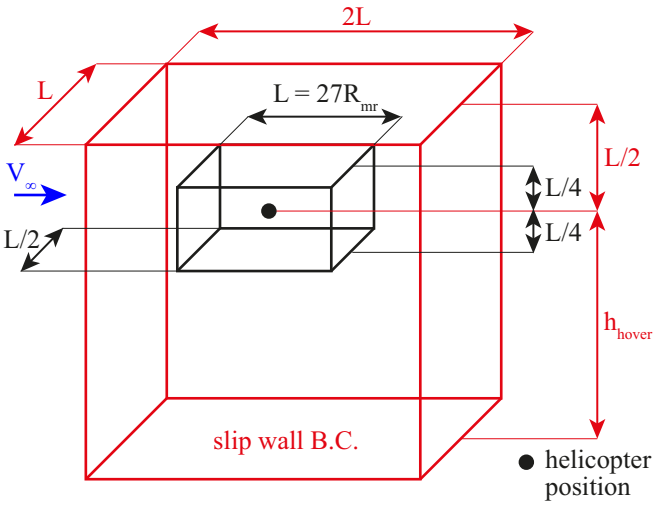

Fig. 3: Comparison of the domain for the cruise and autorotation condition and enlarged domain for the hover condition.

Compressible RANS CFD simulations were performed on the high-performance computing facility at the National Aerospace Laboratory NLR, using the multiblock structured solver ENFLOW (Refs. 10, 11). The equations were solved 2nd order accurate, were discretized in space by a cell-centered finite-volume method using central differences and artificial diffusion, and were integrated in time by an implicit scheme, using the dual-time stepping method. A timestep equivalent to 1° of propeller rotation was used as commonly found in propeller research (Refs. 12, 13). An algebraic Reynolds-stress turbulence model EARSM (Ref. 14) was selected for most simulation cases, except for a number of the cases in the hover condition, for which the $k-\omega$ SST turbulence model (Ref. 15) was used to promote convergence. These exceptions are highlighted in the paper and a comparison between the two turbulence models is also provided.

The multiblock structered grid consisted of about 153 million cells in the cruise and autorotation condition and about 163 million cells in the hover condition. Due to the larger domain and the need for a different first layer thickness, the grid size of the hover condition was slightly larger. In order to comply with the turbulence models, the dimensionless wall distance y^+ on all no-slip walls of the model was less than one.

PERIODICITY AND GRID CONVERGENCE

Solutions of the aerodynamic loading were expected to be in general periodic with the propeller blade passage frequency. In order to obtain such periodic solutions for the cruise and autorotation condition, first a steady solution was obtained on a coarse grid. This was then used as initial condition for time dependent simulations on the coarse, medium refined and at last the fine grid with a timestep equivalent to 1° of propeller rotation, using the solution on one grid level down as initial condition. The coarse and medium refined grids were obtained by structured grid coarsening, reducing the number of cells by a factor of 8. The hover condition required a different recipe to avoid divergence in the solver and to reach periodic behaviour with the blade passage frequency. A steady solution on the fine grid was obtained from steady solutions on the medium refined and coarse grid. This was used as initial condition for a time dependent simulation on the fine grid, advancing quickly in time with a timestep equivalent to 10° of propeller rotation. It was found that to reach periodic behaviour for this flight condition, many propeller rotations were required. At last, a simulation on the fine grid with a timestep equivalent to 1° of propeller rotation was used to obtain the final solution.

In Figure 4 convergence of the most important aerodynamic loading quantities is shown by taking the mean and amplitude of the quantities for each blade passage, subtracted by their values for the last blade passage. Only convergence of the part of the simulation with a timestep equivalent to 1° is shown. The selected quantities are the left propeller thrust coefficient C_T and power coefficient C_P, and the airframe lift coefficient C_L and drag coefficient C_D. For the cruise condition, shown in Figure 4 (a), sufficient convergence to a periodic solution was obtained after two propeller rotations or 12 blade passages on the fine grid. Especially the airframe lift and drag required some time to converge, due to modelling of the exhausts on the fuselage without active flow, resulting in some flow separation. In the hover condition, the flowfield is almost entirely induced by the main rotor and the propellers, resulting in a very large inflow angle to the wings, and large wakes below the wings due to flow separation. Note that for this condition, the lift and drag coefficient are defined with the theoretical downwash velocity in the far field:

$$V_d = \sqrt{\frac{2T_{\text{mr}}}{\rho_\infty \pi R_{\text{mr}}^2}} \tag{1}$$

In the convergence plots in Figure 4 (b) poor convergence with the blade passage frequency is observed for the mean of the airframe lift and to a lesser extent the drag. Instead, a fluctuation with a much lower frequency is observed, likely related to the time variation of the flow separation. However, the amplitude does show convergence. For the propeller coefficients better convergence is obtained. In the autorotation condition the mean propeller thrust was trimmed to zero and therefore the mean of the propeller quantities are very small. The amplitude shows satisfactory convergence. The wing quantities

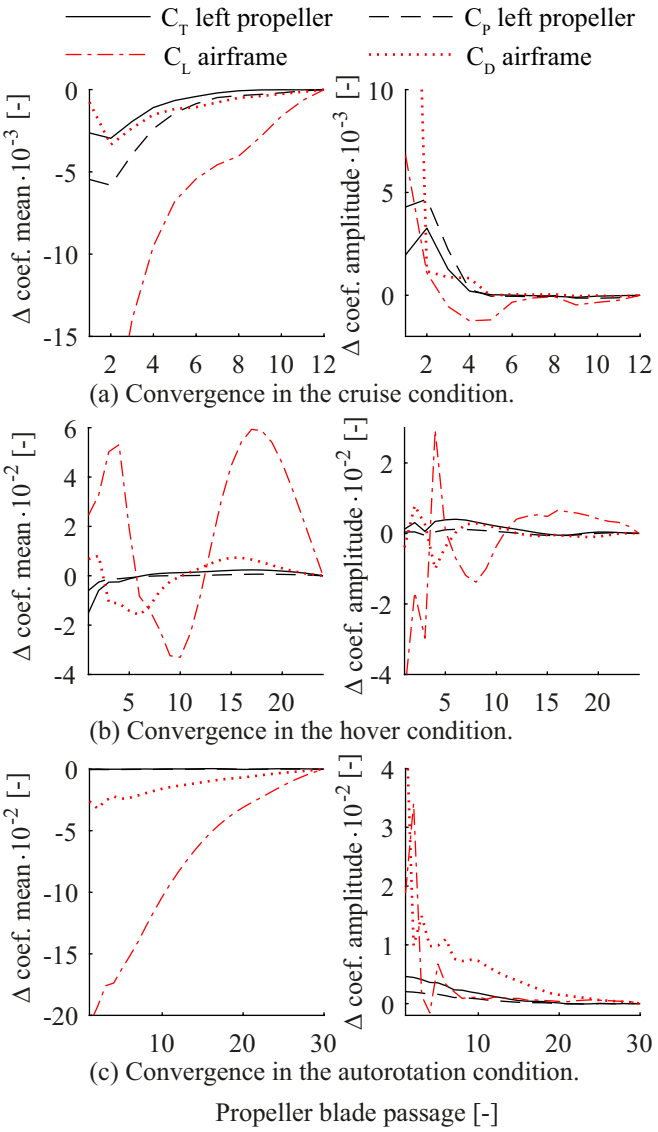

Fig. 4: Convergence plots obtained by calculating mean and amplitude for each blade passage, and subtracting last value.

required three more propeller rotations to converge compared to the cruise condition due to the large angle of attack for this condition.

Since the grid was refined in a structured manner and the solver is 2nd order accurate, grid-dependent uncertainties based on Richardson extrapolation could be calculated, using solutions on the medium refined and fine grid. These are given in Table 1 for the mean over the last blade passage of discussed aerodynamic loading quantities. In the cruise and hover conditions the uncertainties estimated for the propeller quantities are relatively small. For the airframe lift and drag, somewhat larger uncertainties are estimated. In the cruise condition, this is mainly due to the earlier mentioned flow separation from the exhausts on the rear of the fuselage without active flow. In the hover condition, the largely separated flow on the wings due to the very large inflow angle is the main cause of uncertainty. For the autorotation condition the thrust coefficient uncertainty is given absolute since the thrust is trimmed to zero for this condition. A small uncertainty in C_T is found. Also the power coefficient is relatively small in this condition which explains the somewhat larger uncertainty. The uncertainty in airframe lift is found to be larger than in the cruise condition, likely due to the large inflow angle in this condition.

Table 1: Grid-dependent uncertainty of selected quantities.

		cruise	hover	autorotation
left propeller	E_{C_T}	0.2%	0.4%	$3.0 \cdot 10^{-5}$ [a]
	E_{C_P}	0.0%	0.5%	4.5%
airframe	E_{C_L}	1.6%	2.3%	5.1%
	E_{C_D}	6.2%	11.1%	0.8%

[a] Absolute error given because of almost zero mean

RESULTS

Three conditions were investigated: cruise, hover and autorotation. For each of these conditions multiple cases were considered. For the cruise condition, the effect of flap deflection was of main importance. This directly changes the ratio of wing lift to main rotor lift and indirectly affects propeller performance. At zero angle of attack, three flap deflections were studied, $\delta_f = -3°$, $0°$ and $5°$. In the hover condition the propellers are not used for forward thrust but for counter-torque and manoeuvring. Therefore a number of cases with different thrust levels on the left and right propellers were investigated for $\delta_f = 0°$ in a hot and high condition. In the autorotation condition the propeller power should be low. The installation effects on the propeller power were investigated at zero propeller thrust for a positive angle of attack and $\delta_f = -5°$.

Cruise Condition

In the cruise condition the main rotor is slowed down and a considerable portion of the lift comes from the box-wings. Both propellers are utilized for forward thrust. As explained in Figure 2 (a), in the cruise condition the main rotor slipstream does not directly interfere with the propellers, but the main source of interference comes from the upstream wings. In Figure 6 the left propeller thrust and power are plotted over a blade passage starting from the orientation defined in Figure 5. The thrust and power are plotted relative to the time-averaged thrust and power for $\delta_f = 0°$. For the three flap deflections the blade pitch was adjusted to achieve the same time-averaged thrust. A small peak-to-peak fluctuation of 1.5% to 2.5% in thrust is present. This fluctuation increases with increasing flap deflection. A clear effect of the wingtip vortex energy recovery can be noticed in the propeller power curves, as with increasing flap deflection the time-averaged power reduces. Following the fluctuations in thrust, the fluctuations in power also increase with increasing flap deflection and are of similar magnitude.

Figure 7 highlights the wingtip vortex recovery effect, showing the gain in propeller propulsive efficiency with respect to

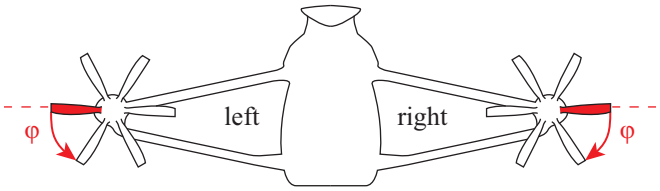

Fig. 5: Rear view of helicopter with blade phase angle definition for the left and right propeller.

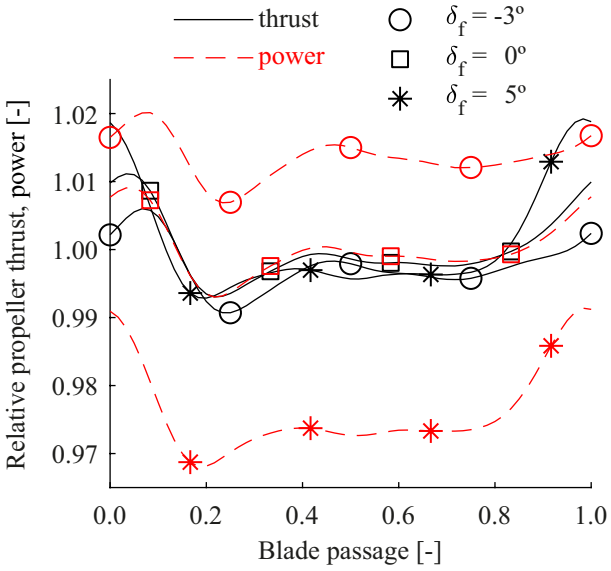

Fig. 6: Left propeller performance in the cruise condition relative to the time-averaged performance for $\delta_f = 0°$. The zero blade passage orientation is defined in Figure 5.

the isolated propeller efficiency at equal thrust. The propulsive efficiency η_p is defined as the ratio of useful work to shaft power. This gain is plotted for the left and right propeller against the lift coefficient of the corresponding wing-half. The change in lift coefficient was achieved by flap deflection. Clearly, installation results in a considerable propulsive efficiency gain for both propellers, becoming larger with increasing wing lift. Increasing the wing lift will allow further unloading of the main rotor and therefore the ratio of wing lift to main rotor lift has a large influence on the efficiency of the propellers.

In order to investigate the source of the propeller installation effects, the blade section thrust and efficiency are plotted in Figure 8 for the left propeller during a complete revolution for $\delta_f = 0°$. These distributions can be correlated to the flowfield just upstream of the propeller, given in contour plots in Figure 9. The axial and tangential velocity components are plotted relative to the freestream airspeed and an approximate section incidence angle is computed, defined as the angle between the velocity vector formed by the axial and tangential velocity component and the local section chordline. The tangential velocity is defined around the propeller rotation axis and is positive in the direction of rotation. The wake of the wings are visible in the axial velocity plot and especially behind the

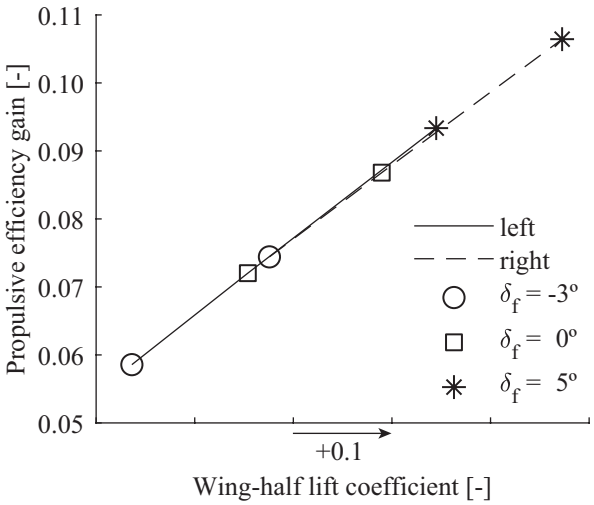

Fig. 7: Propeller propulsive efficiency gain of installation versus the wing-half lift in the cruise condition.

flap gaps a velocity deficit is present. In the thrust contour plot the effect of the wing wakes is clearly visible in a local increase in thrust, resulting in a maximum coinciding with the upper wing wake.

In the tangential velocity plot the rotation of the flow around the nacelle is visible, induced by the loading on the wings. A peak in negative tangential velocity is present on the inboard side of the nacelle near the top. It is known from Patterson and Bartlett (Ref. 4) that this tangential velocity component is the main contributor to the increased efficiency of wingtip mounted pusher propellers. This is confirmed by the current calculation, since there is a clear correlation with the blade section efficiency distribution. The distribution of tangential velocity over the propeller disk can be used to design the propeller to optimally make use of this effect in the cruise condition, producing thrust where the efficiency is highest.

The combined effect of the axial and tangential velocity components can be observed in the blade section incidence angle. An increase in axial velocity and a decrease in tangential velocity results in an increase in incidence angle. While Figure 6 only showed a small variation in propeller thrust, the peak-to-peak variation in blade thrust is much higher due to these local variations in incidence angle and is in the order of 70% of the mean. The resulting cyclic bending moments on the blades need to be taken into account in their structural design.

In order to observe what happens to the flowfield when it passes the propeller, Figure 10 gives an approximation of the tangential velocity component and total pressure through the streamtube of the left propeller. A comparison is made between the installed propeller and isolated propeller at equal thrust. The streamtube was approximated by a cylinder with a radius equal to the propeller radius and quantities were time- and space-averaged over disks from $3R_p$ upstream to $3R_p$ downstream of the propeller. In case of the isolated propeller only the nacelle was present. Upstream of the propeller, the main difference between the installed and isolated flow-

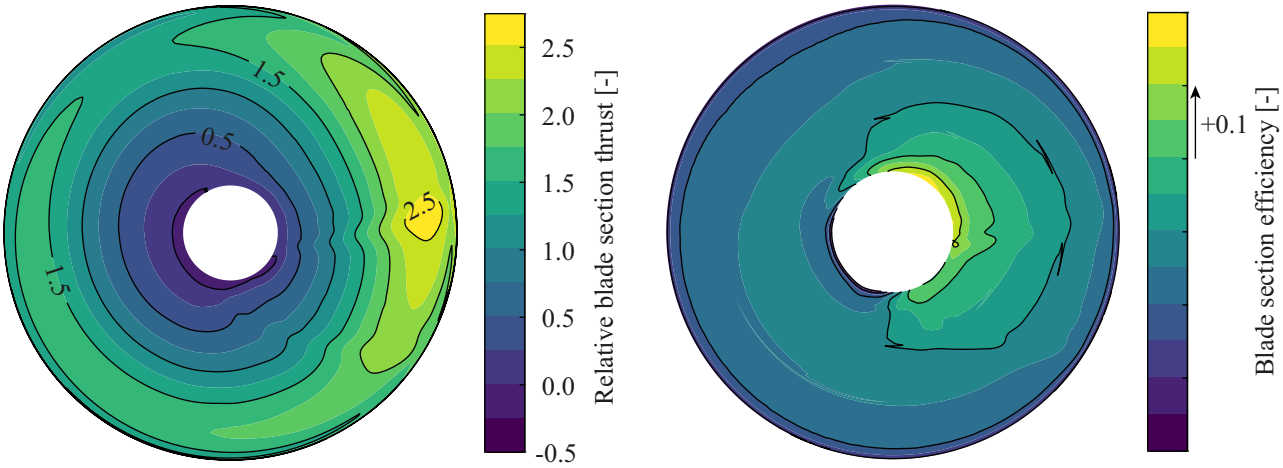

Fig. 8: Contour plots of propeller blade section thrust and efficiency distribution during one complete revolution for the left propeller in the cruise condition for $\delta_f = 0°$. The thrust distribution is plotted relative to the propeller blade thrust time-averaged over the full rotation.

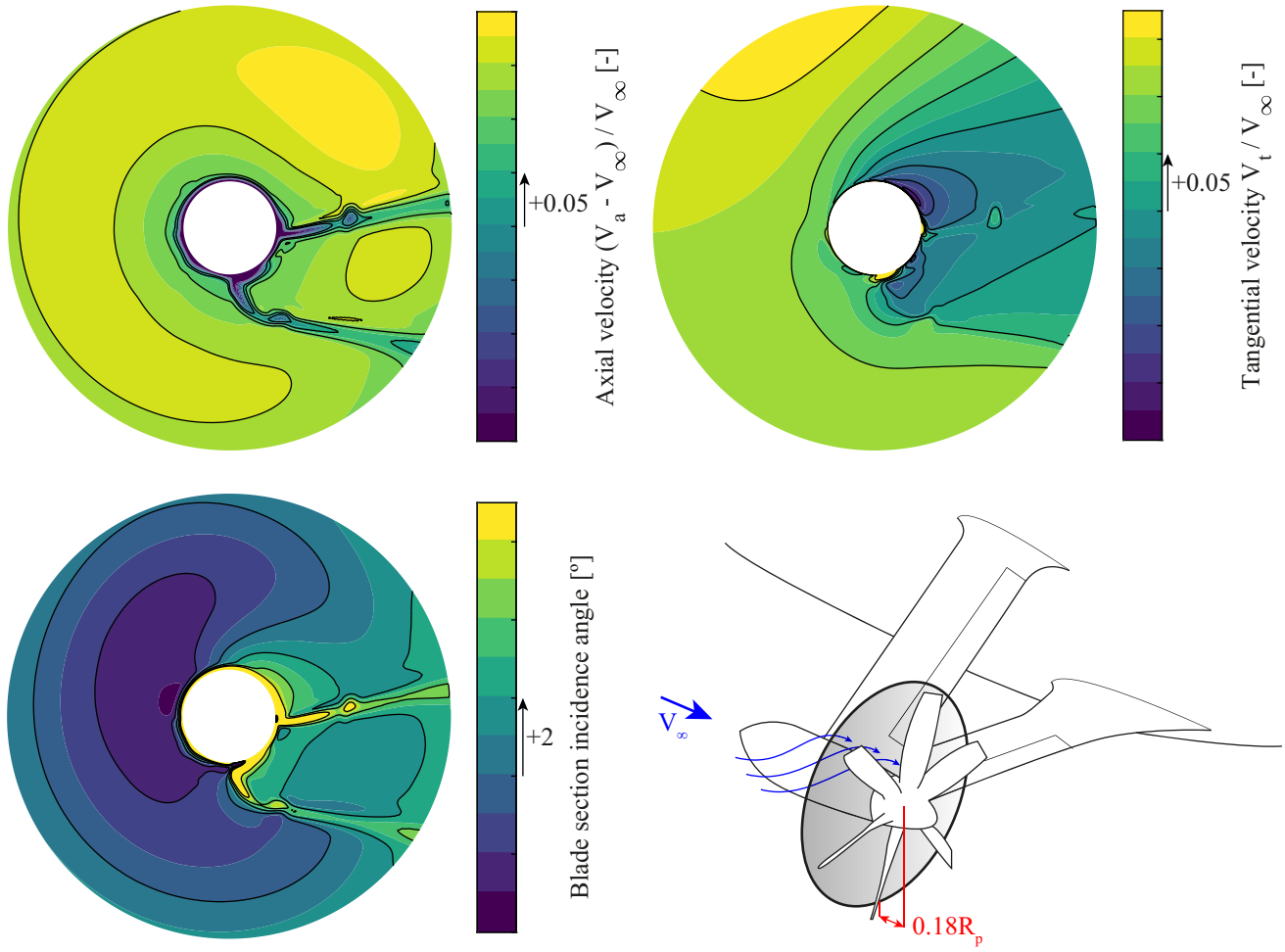

Fig. 9: Contour plots of time-averaged velocity components and blade section incidence angle at a plane $0.18R_p$ upstream of the left propeller in the cruise condition for $\delta_f = 0°$.

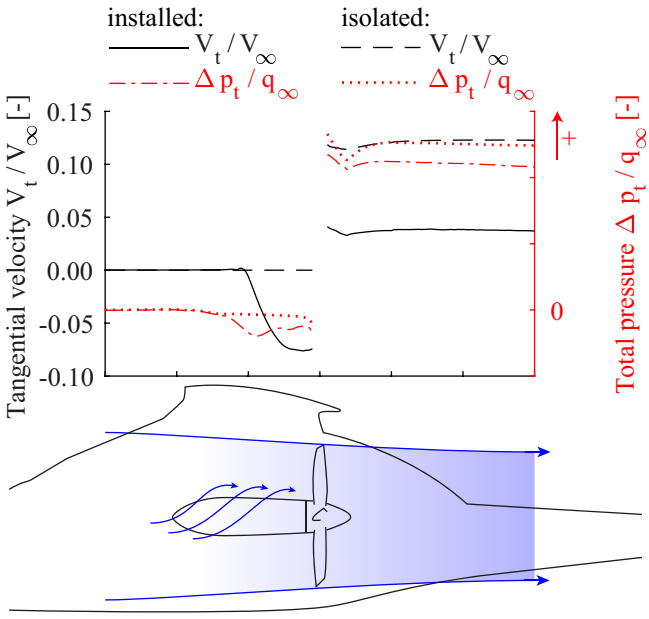

Fig. 10: Time- and space averaged flow quantities through propeller approximate slipstream tube (tube of fixed radius equal to R_p) of installed propeller for $\delta_f = 0°$ and isolated propeller at equal thrust.

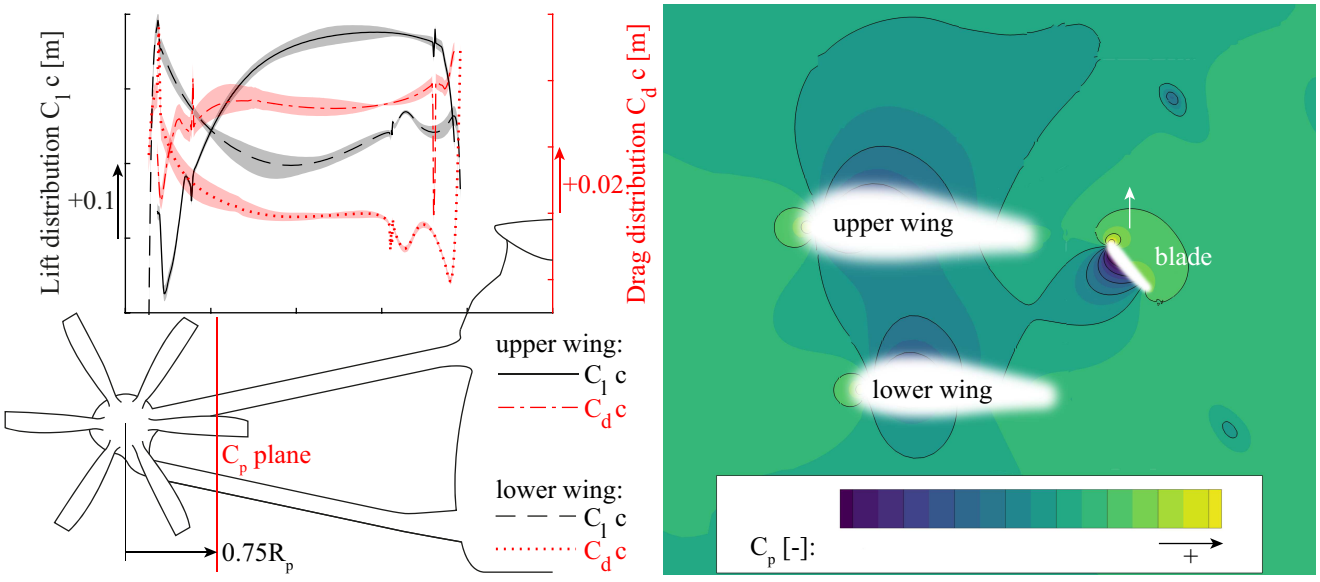

(a) Spanwise lift and drag distribution.

(b) Instantaneous pressure distribution in C_p plane.

Fig. 11: The upstream effect of the left propeller on the box-wing is highighted in the cruise condition for $\delta_f = 0°$. The time-averaged lift and drag distribution are shown in (a) with the variation in time indicated by the shaded areas. The distribution of static pressure in a plane cutting the wings and a propeller blade is shown in (b).

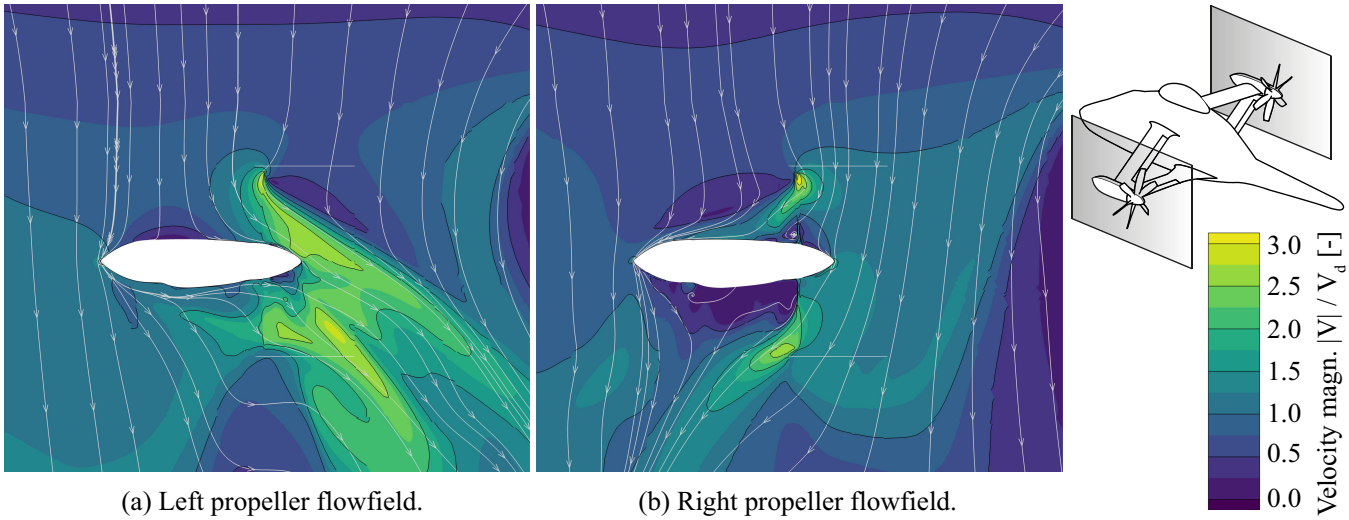

(a) Left propeller flowfield. (b) Right propeller flowfield.

Fig. 12: The time-averaged flowfield is shown in vertical planes coincident with the propeller axes in hover.

field can be found in the growth in negative tangential velocity component towards the propeller as a result of the loading on the wings and the associated static pressure difference between the pressure side of the lower wing and suction side of the upper wing. The total pressure upstream of the propeller reduces for the installed case due to boundary layer growth on the wings. The differences upstream of the propeller impact the slipstream of the propeller: The tangential velocity component is considerably lower for the installed propeller downstream of the propeller. The total pressure is lower as well, and this is directly related to the lower power consumption and thus lower momentum change across the propeller plane.

The box-wings not only affect the propeller performance, there is also a small upstream effect of the propellers on the wing loading in the cruise condition. This upstream effect for the left wing is highlighted in Figure 11 for $\delta_f = 0°$. In Figure 11 (a) the time-averaged spanwise lift and drag distribution are plotted including the variation in time. This variation in time is a direct result of the propeller blades passing by and amounts to a peak-to-peak variation of 1.4% and 6.3% in terms of integrated wing lift and drag respectively. In Figure 11 (b) the static pressure is plotted at an instance in time on a plane cutting through the wings and one of the propeller blades. The region of low pressure on the suction side of the propeller blade extends to the upstream wings and has a varying impact on the pressure distribution of the wings, dependent on the propeller orientation. There is likely also an effect of the propeller on the time-averaged wing loading, but that cannot be determined from the current set of simulations and will be analysed in future work.

Hover Condition

In the hover condition the main rotor generates all of the lift. The propellers are utilized for counter-torque and manoeuvring, with the right propeller producing reverse thrust. Propeller interference in the hover condition differs entirely from the cruise condition: The propellers and the box-wings are in the slipstream of the main rotor as sketched in Figure 2 (b). This induces a net download on the wings and introduces a very non-uniform inflow to the propellers. This time-averaged inflow to the left and right propeller is illustrated in Figure 12 (a) and (b) respectively by a velocity contour plot with streamlines on a vertical plane coinciding with the propeller axis. The inflow to the propellers is near perpendicular to the propeller axes, only deviating because of the influence of the wings and the induced velocity field of the propellers. While the inflow to the left propeller is disturbed by the wings, for the right propeller it is unobstructed. For the right propeller the propeller induces mainly a reverse axial flow and thus reverse thrust near the tip of the blades. This is characteristic of propellers in reverse thrust due to the twist distribution which is not tailored to reverse thrust.

Similar to Figure 9 for the cruise condition, the time-averaged inflow to the left propeller is shown in more detail in Figure 13 with a contour plot of the axial and tangential velocity component. Maxima in axial velocity component can be observed at the location of the wings due to their deflection of the main rotor flow. This opposes the inflow in the cruise condition, where the wing wake resulted in a locally reduced axial inflow. The tangential velocity contour is dominated by the inflow from the main rotor, resulting in a change in sign between the inflow on the inboard and outboard side of the propeller.

The corresponding propeller blade loading response can be found in Figure 14. Results are shown for the two turbulence models used in the hover condition. The results with the EARSM model correspond to the discussed flowfield plots. Both blade thrust and power vary sinusoidally as a result of the tangential velocity component distribution in the inflow. A small deviation from this sinusoidal behaviour is observed between 90° and 180°, caused by the increased axial inflow from the wings. Although not quantified in Figure 14, the

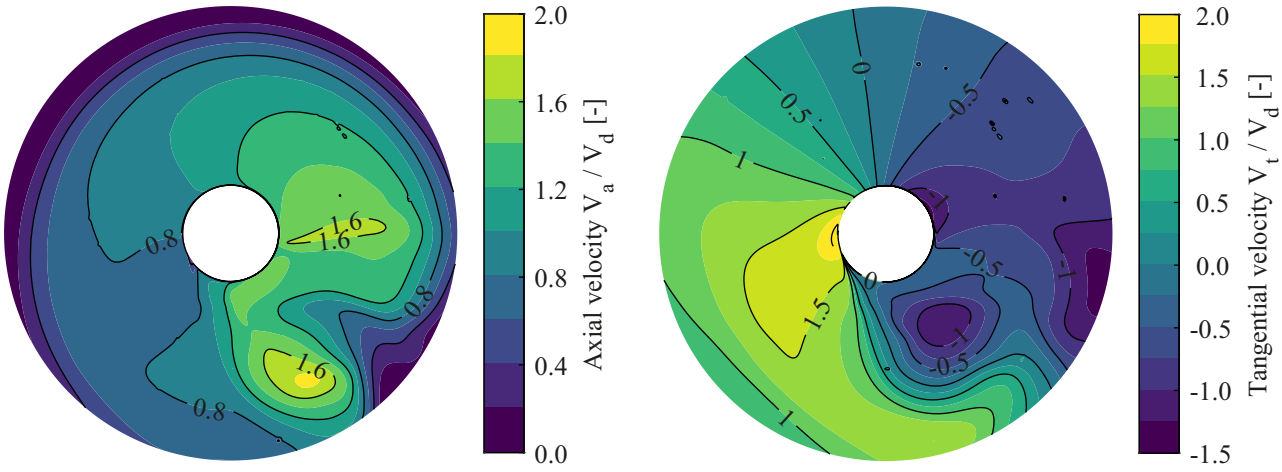

Fig. 13: Contours of time-averaged velocity components at a plane $0.18R_p$ upstream of the left propeller in hover.

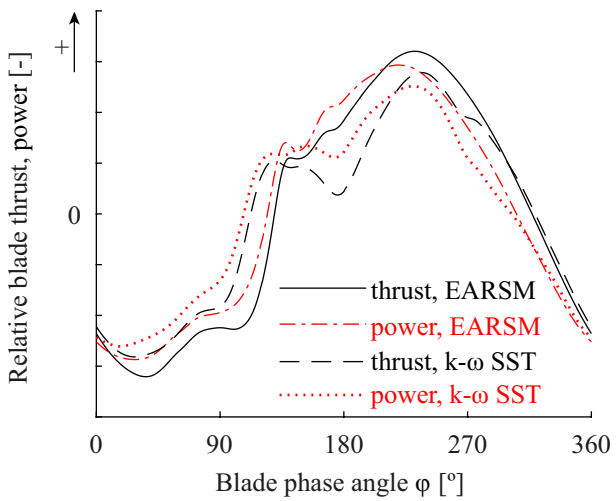

Fig. 14: Propeller blade performance in hover during one full rotation relative to the time-averaged performance. The blade phase angle is defined in Figure 5.

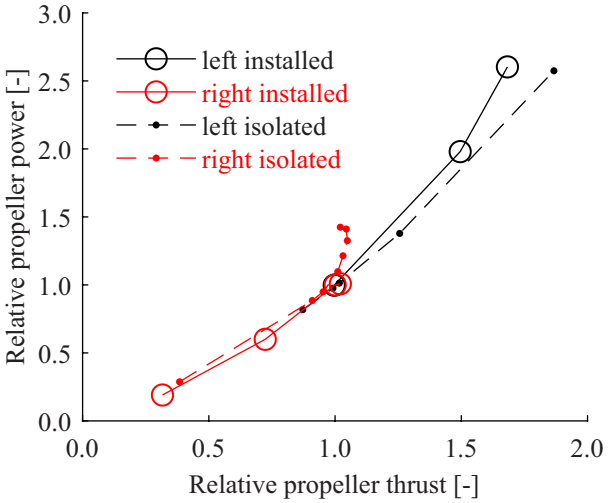

Fig. 15: The propeller performance of the left and right propeller in installed and isolated condition, relative to the installed performance of the nominal hover case.

peak-to-peak variation in blade thrust and power is very significant. The effect of the turbulence model on the blade thrust and power response is relatively small and mainly noticeable in the deviation from the sinusoidal behaviour. This points to the effect of the wings on the inflow to the propeller, which is very likely different due to the flow separation and large wakes below the wings that are expected to be dependent on turbulence modelling.

The previous results are for a condition of 50% higher than nominal thrust for the left propeller and nominal thrust for the right propeller. For the exploration of extreme trimming cases in the hover condition, a range of thrust targets and corresponding blade pitch angles were considered, and the resulting propeller performance is summarized in Figure 15 in a power versus thrust plot. Isolated propeller performance in static condition is also plotted to show the installation effect on the propeller performance. From the isolated propeller performance a drawback of operating a propeller in reverse thrust becomes clear: the maximum achievable thrust is much lower since the non-optimal twist distribution of a propeller in reverse thrust results in early stall. The installation effect for this right propeller is very small. However, for the left propeller a clear reduction in propeller efficiency is found for higher than nominal thrust. It is a consequence of the large variation in blade loading over a rotation: In a part of the rotation the propeller blade sections operate in the non-linear part of the lift curve and may experience a stall-unstall phenomenon when the thrust is even higher.

For a blade orientation close to the maximum in thrust for the left propeller, $\varphi = 230°$, Figure 16 shows a comparison of the

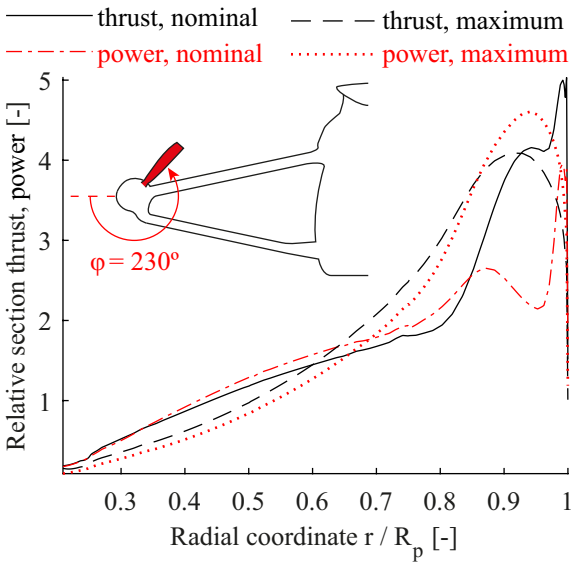

Fig. 16: Radial thrust and power distribution comparison for the nominal and maximum thrust hover cases, plotted w.r.t. the time-averaged blade performance, at $\varphi = 230°$ as defined in Figure 5.

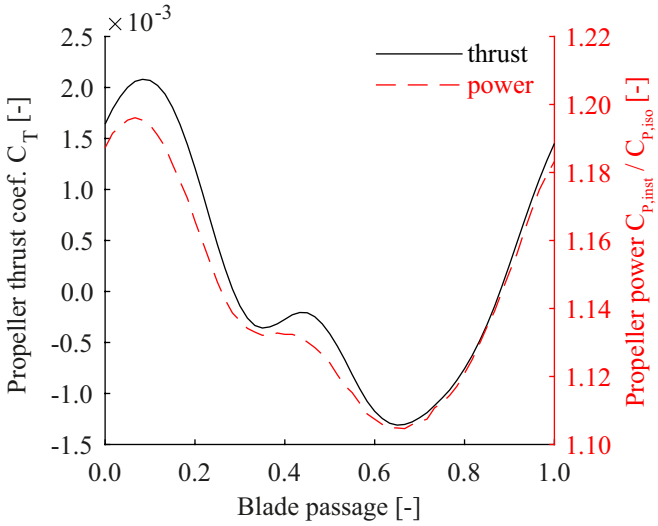

Fig. 17: Left propeller performance in the autorotation condition. Power is given relative to the isolated propeller power at equal thrust. The zero blade passage orientation is defined in Figure 5.

section thrust and power distribution over the radius. Results for both the nominal as well as for the maximum thrust case are plotted relative to the time-averaged blade thrust of that case. The peak in thrust at the outboard portion of the blade for the nominal case has disappeared for the maximum thrust case due to stall at the blade tip and the blade is instead loaded more inboard. As a consequence of the stall, the power associated with the outboard sections is also much higher than for the nominal case. This results in the described installation penalty. Phenomena related to stall come with increased uncertainty in RANS simulations and therefore investigation into this stall-unstall phenomenon including experimental validation is ongoing and these results are therefore not definitive.

Autorotation Condition

In the autorotation condition the propeller power is the main parameter of interest. It should be low enough for the helicopter to sustain the power balance during autorotation. An evaluation was made of the installation effect on the propeller power at zero propeller thrust in a dive with a positive angle of attack and the flaps set at $\delta_f = -5°$. In Figure 17 the left propeller thrust coefficient and the propeller power relative to the isolated propeller power is plotted for one blade passage. The isolated propeller performance was established with nacelle at zero angle of attack. The average propeller thrust was trimmed to be close to zero by varying the blade pitch angle. A small sinusoidal variation in propeller thrust is present. For the propeller power an installation penalty is found over the whole blade passage with an average of 14.4%. The propeller power variation is similar to that of the thrust coefficient.

In order to investigate the source of this power installation penalty, in Figure 18 the section incidence angle in the inflow to the left propeller and corresponding the blade section power are plotted over the propeller disk. The inflow has a number of similarities to that of the cruise condition shown in Figure 9. The wing wakes result in a local strong increase in incidence angle. Furthermore, the wings induce a tangential velocity field which increases the incidence angle and is especially present close to the nacelle. This positive incidence angle results in forward thrust and in order to achieve zero propeller thrust, the blade pitch angle was reduced such that the outboard blade sections experience a negative incidence angle and corresponding reverse thrust. As a result, the propeller power is distributed highly non-uniform and the propeller experiences the described installation penalty.

CONCLUSIONS

In the cruise condition, installation resulted in very efficient propeller operation. The main aerodynamic interaction in this condition was between the wings and propellers. A strong positive correlation was found between wing lift and propeller efficiency. While the propeller experienced only small variations in loading over time, the individual blade loading varied with 70% of the mean during a rotation as a result of this interaction. As a result of the propeller static pressure field, a small variation in wing lift and drag was found of 1.4% and 6.3% respectively.

In the hover condition, a large variation in the propeller blade loading was present, mainly as a result of the near perpendicular inflow due to the main rotor slipstream. In the exploration of extreme trimming cases it was found that for high propeller thrust conditions the blade sections operated partially in the non-linear part of the lift curve and may experience a stall-unstall phenomenon for a non-optimised blade design, reducing time-averaged propeller efficiency. Phenomena related to

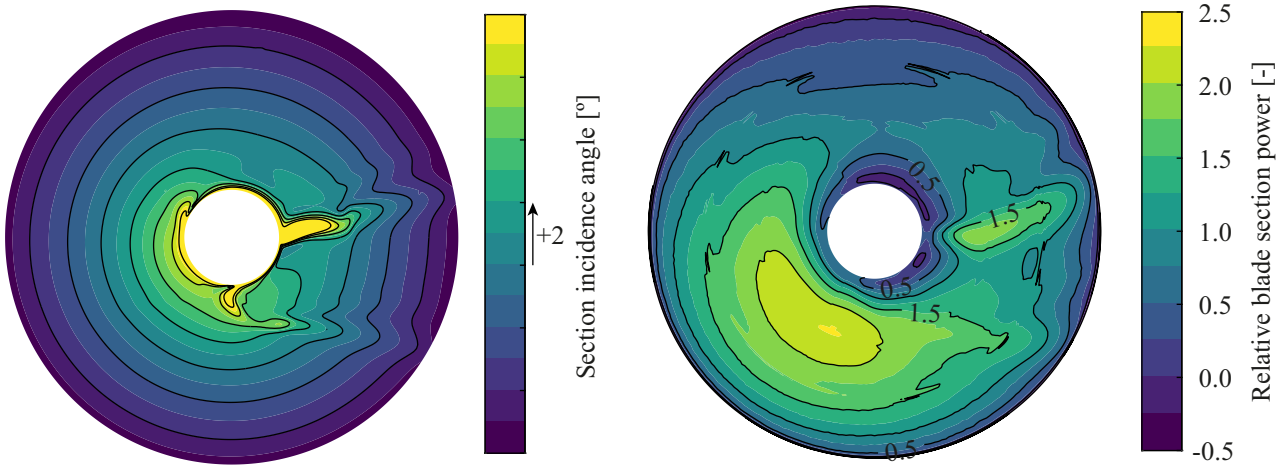

Fig. 18: Contour plot of the blade section incidence angle $0.18R_p$ upstream of the left propeller and the corresponding section power distribution relative to the time-averaged blade loading in the autorotation condition.

stall come with increased uncertainty in RANS simulations and therefore investigation into this stall-unstall phenomenon including experimental validation is ongoing and these results are therefore not definitive.

Furthermore in the hover condition, the right propeller was in reverse thrust to generate a counter-torque. The maximum achievable thrust was therefore much lower since the non-optimal twist distribution of a propeller in reverse thrust results in early stall at the blade tips.

In the autorotation condition, a small installation penalty in terms of propeller power should be considered. This was mainly attributable due to the large range of blade section incidence angles over the propeller disk, resulting in locally forward and reverse thrust.

In general, it can be concluded that propeller performance installation effects for a compound helicopter with wingtip-mounted pusher propellers are highly beneficial in cruise. Drawbacks mainly appear in extreme and specific cases yet these do not question the performance. The resulting dynamic loads are taken into account in the design of the dynamic assemblies. Propeller blade optimisation in future work may mitigate some of these drawbacks.

ACKNOWLEDGMENTS

The authors would like to thank Michel van Rooij from NLR for the preparation of the computational grids. This project has received funding from the Clean Sky 2 Joint Undertaking under the European Unions Horizon 2020 research and innovation programme under grant agreement No 685569 PROPTER H2020-CS2-CFP01-2014-01/H2020-CS2-CFP01-2014-01. This paper reflects only the author's view and the JU is not responsible for any use that may be made of the information it contains.

REFERENCES

[1]Yeo, H. and Johnson, W., "Optimum design of a compound helicopter," *Journal of Aircraft*, Vol. 46, (4), 2009, pp. 1210–1221.

[2]Hirschberg, M., "Clean Sky 2 Update, Part 1: The Airbus Racer," *Vertiflite*, Vol. 63, (5), 2017, pp. 26–28.

[3]Orchard, M. and Newman, S., "The fundamental configuration and design of the compound helicopter," *Proceedings of the Institution of Mechanical Engineers, Part G: Journal of Aerospace Engineering*, Vol. 217, (6), 2003, pp. 297–315

[4]Patterson Jr, J. C. and Bartlett, G. R., "Effect of a wing tip mounted pusher turboprop on the aerodynamic characteristics of a semi-span wing," AIAA/SAE/ASME/ASEE 21st Joint Propulsion Conference, Monterey, CA, July 1985.

[5]Janus, J. M., Chatterjee, A. and Cave, C., "Computational analysis of a wingtip-mounted pusher turboprop," *Journal of Aircraft*, Vol. 33, (2), 1996, pp. 441–444.

[6]Miranda, L. R., Brennan, J. E., "Aerodynamic effects of wingtip-mounted propellers and turbines," AIAA 4th Applied Aerodynamics Conference, San Diego, CA, June 1986.

[7]Bain, L. J. and Landgrebe, A. J., "Investigation of Compound Helicopter Aerodynamic Interference Effects," US-AAVLABS Technical report 67-44, 1967.

[8]Lynn, R. R., "Wing-rotor interactions," *Journal of Aircraft*, Vol. 3, (4), 1966, pp. 326–332.

[9]Roosenboom, E. W. M. and Schröder, A., "Flowfield Investigation at Propeller Thrust Reverse," *Journal of Fluids Engineering*, Vol. 132, (6), 2010, pp. 061101.

[10]Boerstoel, J. W., Kassies, A., Kok, J. C. and Spekreijse, S. P. "ENFLOW, a full-functionality system of CFD codes for industrial Euler/Navier-Stokes flow computations," NLR Technical publication TP 96286 U, 1996.

[11]Laban, M., Kok, J. C., and Prananta, B. B., "Rotating Open-Rotor Performance, Noise and Vibration Assessment," 27th International Congress of the Aeronautical Sciences (ICAS 2010), Nice, France, September 2010.

[12]Roosenboom, E. W. M. and Schröder, A., "Advanced experimental and numerical validation and analysis of propeller slipstream flows," *Journal of Aircraft*, Vol. 47, (1), 2010, pp. 284–291.

[13]Ortun, B., Boisard, R. and Gonzalez-Martino, I., "In-plane airloads of a propeller with inflow angle: prediction vs. experiment," 30th AIAA Applied Aerodynamics Conference, New Orleans, LA, June 2012.

[14]Wallin, S. and Johansson, A. V., "An explicit algebraic Reynolds stress model for incompressible and compressible turbulent flows," *Journal of Fluid Mechanics*, Vol. 403, 2000, pp. 89–132.

[15]Menter, F. R., "Two-Equation Eddy-Viscosity Turbulence Models for Engineering Applications," *AIAA Journal*, Vol. 32, (8), 1994, pp. 1598–1605.